Surface & Coatings Technology 206 (2011) 1698–1704

Contents lists available at SciVerse ScienceDirect

Surface & Coatings Technology

journal homepage: www.elsevier.com/locate/surfcoat

Phase stability and alloy-related trends in Ti–Al–N, Zr–Al–N and Hf–Al–N systems from first principles

David Holec [a,*], Richard Rachbauer [a], Li Chen [a,b], Lan Wang [a], Doris Luef [a], Paul H. Mayrhofer [a]

[a] Department of Physical Metallurgy and Materials Testing, Montanuniversität Leoben, Franz-Josef-Strasse 18, A-8700 Leoben, Austria
[b] State Key Laboratory of Powder Metallurgy, Central South University, Changsha Hunan, 410083, China

ARTICLE INFO

Available online 17 September 2011

Keywords:
Density functional theory (DFT)
Hard coatings
TiAlN
ZrAlN
HfAlN

ABSTRACT

Transition metal aluminium nitride (TM–Al–N) thin films are valued for their excellent mechanical (e.g. hardness) as well as protective (e.g. oxidation resistance) properties. This paper addresses the structure and phase stability of group IVB TM–Al–N systems $Ti_{1-x}Al_xN$, $Zr_{1-x}Al_xN$, and $Hf_{1-x}Al_xN$. The predicted stability regions of the rock salt cubic structures are $x \leq 0.7$, $x \leq 0.45$, and $x \leq 0.45$, respectively, while the wurtzite-type single phase field is obtained for $x \geq 0.7$, $x \geq 0.68$, and $x \geq 0.62$ respectively. The predicted phase stability regions and the broad dual-phase transition regions in the case of $Zr_{1-x}Al_xN$ and $Hf_{1-x}Al_xN$ are validated by experiments. Furthermore, the phase transition from cubic to wurtzite with increasing Al content in the alloys is correlated with changes of electronic structure and bonding in the systems.

1. Introduction

Hard coatings based on TiAlN are well established and routinely used for various industrial applications due to their outstanding properties like high hardness, wear and corrosion resistance [1]. However, these favourable properties are obtained basically for compositions maintaining the cubic (rock salt-type) symmetry while they – with only a few exceptions – deteriorate for high Al-containing coatings adopting the hexagonal (wurtzite-type) phase [2]. Nowadays, many applications demand specially-tailored coating properties and thus call for new materials.

In this study we focus on a comparison of group IVB transition metal nitrides alloyed with aluminium (TM–Al–N, TM = Ti, Zr, Hf) as ZrN and HfN have some material properties superior to TiN. For example, ZrN exhibits lower friction coefficient than TiN and it is relatively hard [3, 4]. On the other hand, HfN has the highest melting point and highest elastic moduli in the TMN family [5, 6].

We employ the density functional theory to investigate the structure of $Ti_{1-x}Al_xN$, $Zr_{1-x}Al_xN$, and $Hf_{1-x}Al_xN$ ternary alloys. In particular, we focus on the cubic B1 (space group $Fm\bar{3}m$, NaCl prototype, further in the text referred to as "cubic" or "c-"), hexagonal B_k (space group $P6_3/mmc$, BN prototype, referred to as "hexagonal" or "h-"), and hexagonal B4 (space group $P6_3mc$, ZnS-wurtzite prototype, referred to as "wurtzite" or "w-") allotropes (see Fig. 1a, b, and c, respectively) as the cubic structure is the stable configuration of the binary TMN compounds while the wurtzite structure is the ground state of AlN. The hexagonal B_k configuration is considered due to its similarity to the wurtzite structure (the c/a ratio shrinks from ≈ 1.6 typical for the wurtzite structure to ≈ 1.2, nitrogen atoms are shifted into the anion planes, thus changing from four to five coordinated neighbourhoods, see Fig. 1d). This phase plays a significant role in understanding, e.g. the extended dual-phase transition region in the NbN–AlN system [7], and has been discussed in other TM–Al–N systems, too [8].

Although the $Ti_{1-x}Al_xN$ system is well reported in the literature, there are only a few reports on $Zr_{1-x}Al_xN$ and $Hf_{1-x}Al_xN$. In this paper we aim to partially fill in this gap by performing a thorough theoretical study to compare the structural properties and phase stability regions in a "coherent" way, and to elucidate the predicted trends in terms of the electronic structure of these alloys.

2. Methods

The individual structures are modelled with supercells constructed using a special quasi-random structure (SQS) approach [9]. All alloys considered in this paper are quasi-binary which means that mixing of elements (either TM or Al) takes place only on one sublattice (bigger atoms in Fig. 1); the other sublattice is fully occupied with N atoms. $3 \times 3 \times 2$ (36 atoms) and $2 \times 2 \times 2$ (32 atoms) supercells were used for the cubic B1 and hexagonal B_k/wurtzite B4 modifications, respectively. The short range order parameters (SROs) were optimised for pairs up to the fourth order, triplets up to the third order and quadruplets up to the second order [10]. More details about the cells and the process of their generation can be found in Ref. [11].

The density functional theory based calculations were performed using the Vienna Ab-initio Simulation Package [12, 13] together

* Corresponding author.
E-mail address: david.holec@unileoben.ac.at (D. Holec).

0257-8972
doi:10.1016/j.surfcoat.2011.09.019

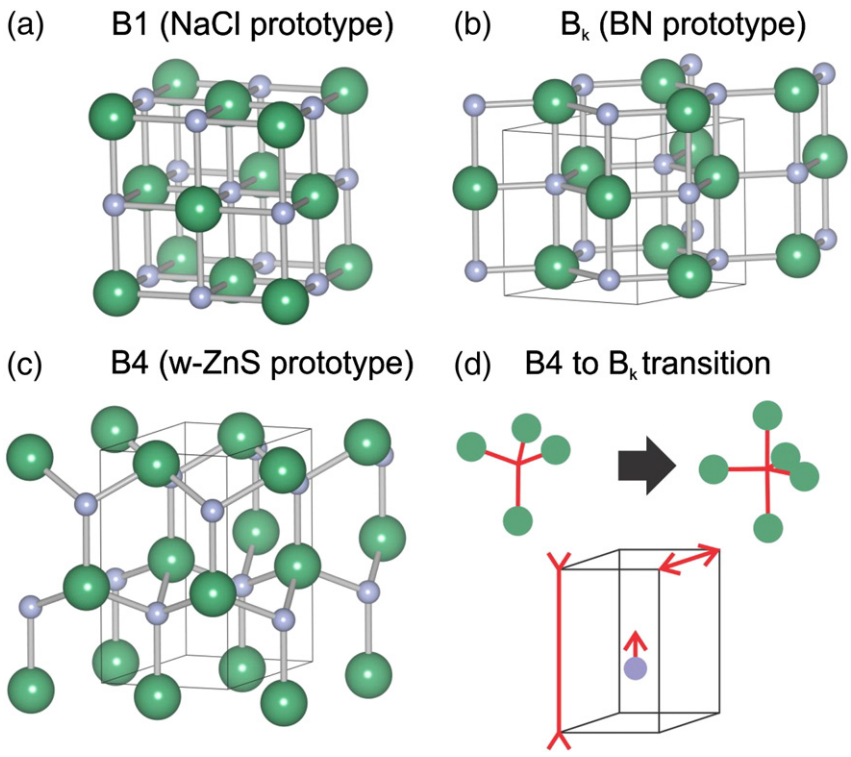

Fig. 1. Crystallographic structures considered in this work: (a) cubic B1, (b) hexagonal B_k, and (c) wurtzite B4. The smaller blue balls represent N atoms while the bigger green spheres correspond to the metallic sites. (d) The structural relationship between the wurtzite B4 and hexagonal B_k phases is illustrated.

with the projector augmented wave pseudopotentials [14] employing the generalised gradient approximation (GGA) as parametrised by Wang and Perdew [15]. We used 500 eV for the plane-wave cut-off energy and a minimum of ≈600 *k*-points·atom (usually more). Such parameters guarantee the calculation accuracy in the order of meV/atom. For several compositions, we checked the energy differences obtained from various supercells with the same SROs. The total energy variations of the cubic B1 structures were far below the here claimed accuracy of the calculations (i.e. below 1 meV/at.), while in the case of hexagonal B_k and wurtzite phases, the different arrangements of atoms result in energy scatter of maximum ±≈15 meV/at. This is caused by the structural similarities of the hexagonal B_k and wurtzite phases as discussed in Section 4.2. Nevertheless, as these differences do not change conclusions for the phase stability, we used one supercell for each composition and crystallographic structure; we used the same set of supercells for all material systems for consistency.

For comparison, three series of samples, $Ti_{1-x}Al_xN$, $Zr_{1-x}Al_xN$, and $Hf_{1-x}Al_xN$, were deposited using the plasma-assisted unbalanced magnetron sputtering technique described in detail in Ref. [16]. The substrate temperature used was ≈500 °C, the total working gas pressure was ≈0.4 Pa, and the N_2 partial pressure ratio for the Ar–N_2 gas mixture was ≈14% of $Zr_{1-x}Al_xN$ and ≈30% for $Ti_{1-x}Al_xN$ and $Hf_{1-x}Al_xN$. The various coatings were deposited by sputtering of powder-metallurgically prepared targets (Plansee SE, $Ti_{0.5}Al_{0.5}$ and $Zr_{0.365}Al_{0.635}$ with the diameter of 150 mm and thickness 5 mm and $Hf_{0.7}Al_{0.3}$, and $Hf_{0.55}Al_{0.45}$ with diameters of 75 mm and thicknesses of 6 mm), and adding various numbers of Al-platelets (∅5 mm × 3 mm) on the target race track. The substrates used were mild steel for Ti–Al–N, stainless steel (AISI 304) for Zr–Al–N, and Si (0 0 1) for the Hf–Al–N system. The chemical composition of the resulting coatings was determined by energy-dispersive X-ray spectroscopy using a Zeiss EVO 50 scanning electron microscope and a TiN coating standard which has been quantified by Rutherford Back-scattering Spectroscopy [17]. All compositions were normalised to 50 at.% N contents. The structure of the coatings was investigated by X-ray diffraction (XRD) using a Bruker AXS D8 Advance diffractometer (Cu K-α radiation) in Bragg–Brentano geometry.

3. Results

3.1. Alloy lattice parameters

For each system, i.e. $Ti_{1-x}Al_xN$, $Zr_{1-x}Al_xN$ or $Hf_{1-x}Al_xN$, and each composition *x*, the equilibrium properties were obtained by optimising the supercell volume and shape as well as internal atomic positions with respect to total energy, using the Birch–Murnaghan equation of state [18]. The resulting lattice parameters for cubic, hexagonal B_k, and wurtzite phases are shown in Fig. 2. The calculated values were fitted with a quadratic polynomial

$$a(x) = xa_{\mathrm{AlN}} + (1-x)a_{\mathrm{TMN}} + bx(1-x) \quad (1)$$

where *b* is a bowing parameter describing the deviation from a linear, Vegard's-like behaviour. In the case of cubic phases, we got $b_{\mathrm{TiAlN}} = 0.064$Å, $b_{\mathrm{ZrAlN}} = 0.230$Å, and $b_{\mathrm{HfAlN}} = 0.197$Å, suggesting that TiAlN exhibits the most linear behaviour out of these three systems. This is, however, a consequence of a smaller difference between the lattice constants of c-AlN and c-TiN as compared with c-AlN and c-ZrN or c-AlN and c-HfN; when *b* is normalised to this difference, $\bar{b} = b/(a_{\mathrm{TMN}} - a_{\mathrm{AlN}})$, similar values of $\bar{b}_{\mathrm{TiAlN}} = 0.36$, $\bar{b}_{\mathrm{ZrAlN}} = 0.42$, and $\bar{b}_{\mathrm{HfAlN}} = 0.43$ are obtained. These imply that the relative increase of the alloy lattice parameter above the linear interpolation of the binary boundary systems is approximately the same for all three systems. It is also worth noting, that the alloy lattice parameter of cubic phases is always predicted to be larger than the linear interpolation.

The *a* lattice parameter of the hexagonal B_k phase is in all three cases almost linear (b<0.05Å) and steadily decreases with increasing AlN mole fraction. The *c* lattice constant remains almost unaffected for $Ti_{1-x}Al_xN$, while it decreases towards the AlN-rich side for $Zr_{1-x}Al_xN$

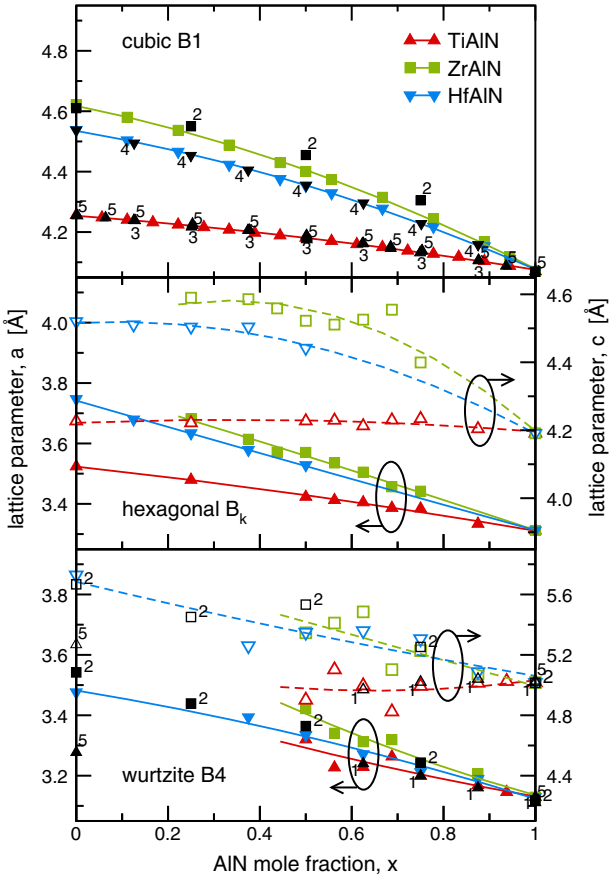

Fig. 2. Lattice parameters for (a) cubic, (b) hexagonal B_k, and (c) wurtzite phases as functions of the alloy composition. Solid symbols and lines correspond to the *a* lattice parameters, while open symbols and broken lines to the *c* lattice parameters. The full black labelled symbols correspond to data from following references: 1 — [19], 2 — [4], 3 — [20], 4 — [21], and 5 — [22].

and $Hf_{1-x}Al_xN$. In both latter cases, the dependence is significantly bowed above the linear relationship: $b_{ZrAlN} = 0.58$Å and $b_{HfAlN} = 0.39$Å.

Finally, the lattice parameters of the wurtzite phase exhibit similar trends to those described for the hexagonal B_k phase: a decrease of the values with increasing AlN mole fraction is predicted. In contrast to the cubic and hexagonal phases, however, the wurtzite lattice parameters of $Ti_{1-x}Al_xN$ and $Zr_{1-x}Al_xN$ show negative bowing parameters (e.g. $b_{TiAlN} = -0.112$Å for the *a* lattice parameter or $b_{HfAlN} = -0.110$Å for the *c* lattice parameter) suggesting that the alloy in the wurtzite form actually takes less space than the respective mixture of the binary counterparts. However, the bowing parameter should not be over-interpreted due the scatter of the calculated lattice constants.

It is worth noting that for low and high AlN mole fractions the wurtzite and hexagonal structures, respectively, become difficult or impossible to stabilise, i.e. that the energy-volume data needed for fitting the Birch–Murnaghan equation of state are too scattered. This is likely due to the structural similarity of these two polymorphs, and the competition between the bonding schemes taking place (see Section 4.2).

The calculated lattice parameters of c- and w-$Ti_{1-x}Al_xN$ agree well with those previously published in the literature [22, 21] and [19], respectively, which are well supported by experimental findings (e.g., [23]). The trends predicted by Sheng et al. [4] for small ordered cells of $Zr_{1-x}Al_xN$, i.e. positive bowing of the lattice parameters as well as a smaller lattice constant change of hexagonal/wurtzite $Zr_{1-x}Al_xN$ at the ZrN-rich end, are confirmed here by using larger and disordered cells and a dense mesh of compositions. The experimental data of Howe et al. [6] confirm our predictions for positive bowing of the c-$Hf_{1-x}Al_xN$ lattice parameter, although the deviation from Vegard's rule predicted here seems to be smaller than that observed experimentally which could, however, be due to residual stresses in the films.

3.2. Phase stability

The energy of formation, E_f, defined as

$$E_f(TM_xAl_{1-x}N) = E_{tot}(TM_xAl_{1-x}N) - \frac{1}{2}\left[xE_{tot}(Al) + (1-x)E_{tot}(TM) + \frac{1}{2}E_{tot}(N_2)\right], \quad (2)$$

expresses the energy gain when the alloy is formed with respect to the individual species (in crystalline form) and molecular nitrogen. Here, the $E_{tot}(X)$ expresses the total energy (output of the calculation) per atom of a respective crystal or molecule *X*. E_f determines which of the three competing phases, i.e. cubic, hexagonal B_k, and wurtzite, is energetically favourable for a certain composition and system (see Fig. 3).

There is a clear and almost single-point cross-over at $x \approx 0.7$ between the cubic and wurtzite polymorphs of $Ti_{1-x}Al_xN$. The hexagonal B_k phase has, within the accuracy of our calculations, at $x \approx 0.7$ the same formation energy as the cubic and hexagonal structures, for other compositions it lies between the cubic and wurtzite phases suggesting that it is never energetically the most favourable phase.

The situation is different for the $Zr_{1-x}Al_xN$ and $Hf_{1-x}Al_xN$ systems as the formation energy of the hexagonal B_k phase overlaps with that of the cubic polymorph in a wide range of concentrations, starting at $x \approx 0.45$. Consequently, the cubic and $B_k$phases are expected to coexist for these AlN mole fractions. On the AlN-rich end ($x \approx 0.68$ for $Zr_{1-x}Al_xN$ and 0.62 for $Hf_{1-x}Al_xN$) of the dual phase region marked in Fig. 3, the E_f of hexagonal and wurtzite phases overlap while the cubic phase has already a notably higher energy. This together with the similarity of the B_k and B4 phases points towards "structural broadness" which will be further discussed in Section 4.2.

In summary, the maximum solubility of AlN in the c-$Ti_{1-x}Al_xN$ is predicted to be at ≈ 0.7 while it is predicted to drop to ≈ 0.45 for c-$Zr_{1-x}Al_xN$ and c-$Hf_{1-x}Al_xN$, followed by a dual phase region up to $x \approx 0.68$ and ≈ 0.62, respectively. For higher AlN mole fractions, the wurtzite phase is the most energetically favourable.

4. Discussion

4.1. Experimental verification of the maximum solubility limit

Several theoretical predictions for the maximum solubility of AlN in c-TM–Al–N systems (TM = Ti, Zr, Hf) have been already published in the literature. Holleck [3] predicted that the transition to the wurtzite phase should occur at ≈ 0.7 for all three system investigated in this paper. Values between 0.67 and 0.7 were predicted for $Ti_{1-x}Al_xN$ [22, 24, 25] using ab initio techniques while a similar approach applied to the $Zr_{1-x}Al_xN$ system yielded a value close to 0.5 [4]. A band parameter based model employed by Makino [26] resulted in $x = 0.65$ for $Ti_{1-x}Al_xN$, $x = 0.33$ for $Zr_{1-x}Al_xN$, and $x = 0.21$ for $Hf_{1-x}Al_xN$.

Experimental observations are consistent with the predictions. Maximum solubility for AlN in c-$Ti_{1-x}Al_xN$ spans a wide range between 0.4 [23] and 0.9 [27], with most of the reports agreeing on values close to 0.7 [27–29]. In c-$Zr_{1-x}Al_xN$, the reported maximum solubility is between 0.37 and 0.43 [30–32], while in c-$Hf_{1-x}Al_xN$ it is at ≈ 0.5 [6,33,34].

Fig. 4 presents X-ray diffraction patterns for $Ti_{1-x}Al_xN$, $Zr_{1-x}Al_xN$ and $Hf_{1-x}Al_xN$ films with different compositions. From the position and the shape of the peaks we can conclude that also our $Ti_{1-x}Al_xN$ coatings are single phase cubic up to $x = 0.62$, dual phase cubic and

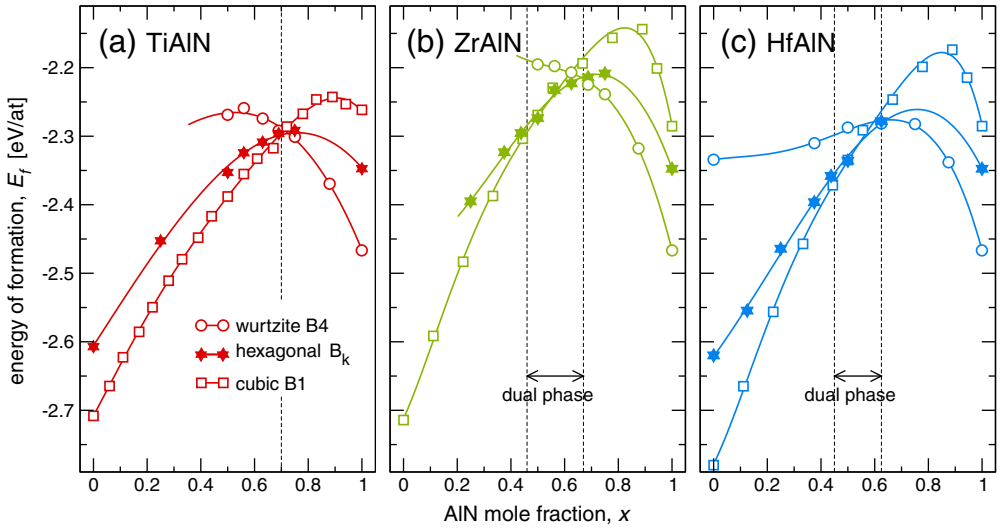

Fig. 3. Energy of formation (E_f) of cubic (square symbols), hexagonal B_k (stars symbols), and wurtzite (circles symbols) structures of (a) $Ti_{1-x}Al_xN$, (b) $Zr_{1-x}Al_xN$, and (c) $Hf_{1-x}Al_xN$ systems. A structure with the lowest energy of formation is predicted to be the most stable one for a particular composition *x*.

hexagonal/wurtzite at $x=0.67$ and single phase wurtzite for $x\geq 0.75$ (see Fig. 4a). $Zr_{1-x}Al_xN$ coatings are single phase cubic up to $x=0.38$ (see Fig. 4b). For $x=0.43$ and $x=0.52$ the cubic peaks get significantly broader and less pronounced indicating a loss of crystallinity and possibly an appearance of a second phase and/or an onset of the isostructural decomposition. The coating with $x=0.62$ crystallised in hexagonal/wurtzite structure. In the case of $Hf_{1-x}Al_xN$, the cubic phase is maintained up to $x=0.33$, between $x=0.38$ and 0.71, an amorphous or nanocrystalline material is obtained (which may be a result of three competing phases and/or again the onset of isostructural decomposition), while at $x=0.77$ a wurtzite single phase field is entered (see Fig. 4c).

Holec et al. [25] discussed an effect of the hydrostatic pressure on the phase stability on $Ti_{1-x}Al_xN$ and $Cr_{1-x}Al_xN$ systems and showed quantitatively, that compressive pressures about 4 GPa cause an increase in x_{max} of about 10%. Therefore, the here presented results should serve for a relative comparison between the systems and for comprehension of the differences between them, rather than as absolute predictions.

4.2. Energy landscape

In order to elucidate the broad dual-phase regions of $Zr_{1-x}Al_xN$ and $Hf_{1-x}Al_xN$ as compared with $Ti_{1-x}Al_xN$, we focused on energy landscapes of the hexagonal/wurtzite phases around the transition point, similar to the analysis of Tasnádi et al. [35] for Sc–Al–N. For a fixed alloy and composition *x*, the *c*/*a* ratio and supercell volume were varied in ranges covering the expected hexagonal B_k and wurtzite B4 structures. For each *c*/*a* ratio and volume, the internal atomic positions were relaxed. The thus obtained energy surface is visualised by contour plots for $Ti_{0.375}Al_{0.625}N$, $Zr_{0.375}Al_{0.625}N$, and $Hf_{0.375}Al_{0.625}N$ in Fig. 5a–c.

In the case of $Ti_{1-x}Al_xN$, a well-defined pronounced minimum corresponding to the B_k phase ($c/a\approx 1.25$) can be seen (Fig. 4a); there is no local minimum related to the wurtzite phase, i.e. the wurtzite

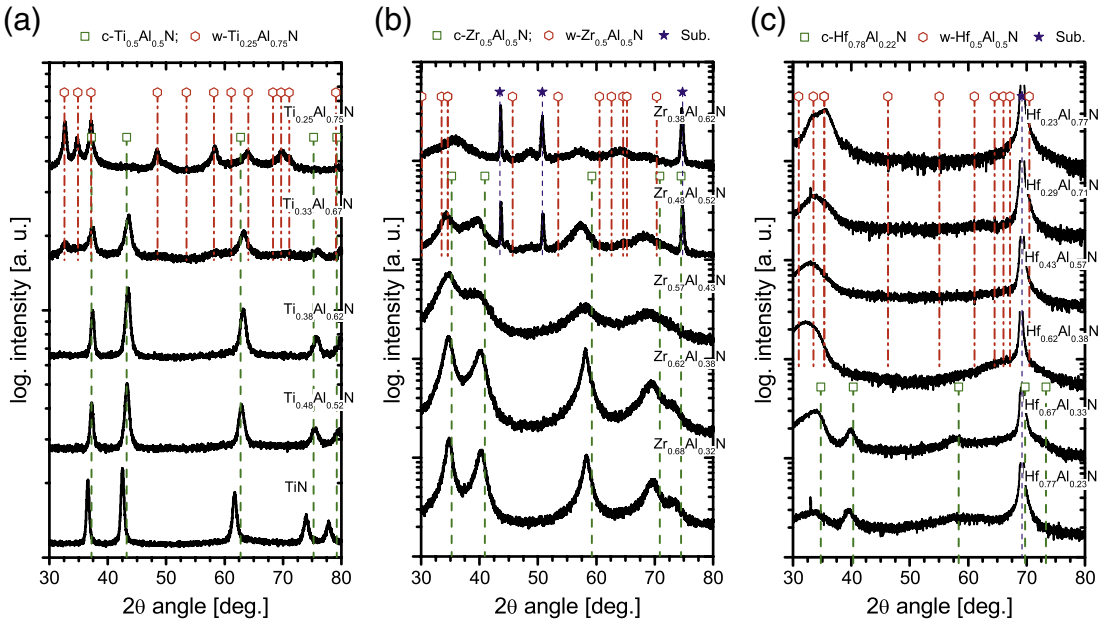

Fig. 4. XRD patterns of (a) $Ti_{1-x}Al_xN$, (b) $Zr_{1-x}Al_xN$, and (c) $Hf_{1-x}Al_xN$ systems as function of the coating composition.

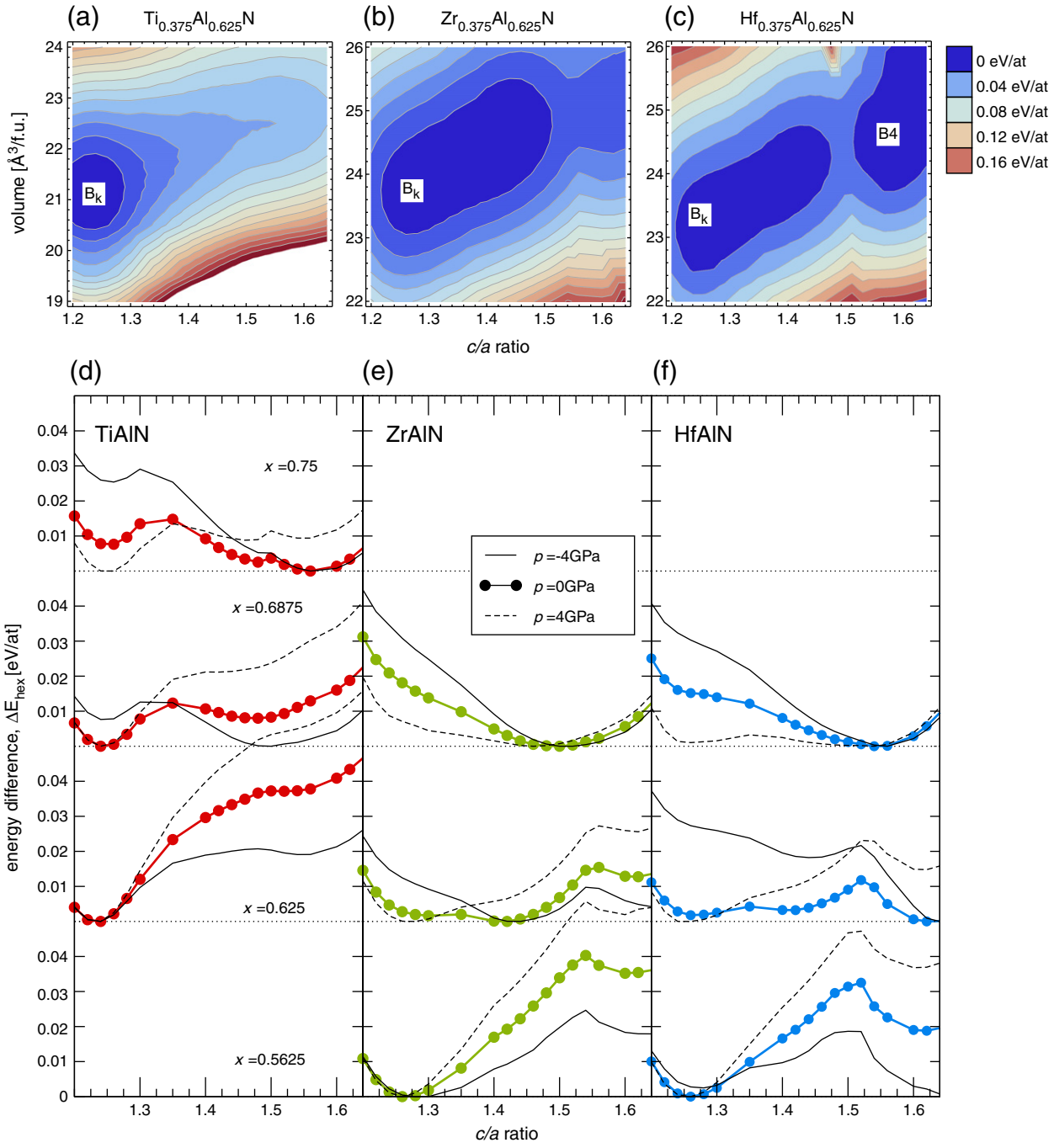

Fig. 5. Energy landscapes for (a) $Ti_{0.375}Al_{0.625}N$, (b) $Zr_{0.375}Al_{0.625}N$, and (c) $Hf_{0.375}Al_{0.625}N$. Energy profiles as functions of the c/a ratio for several AlN mole fraction in (d) $Ti_{1-x}Al_xN$, (e) $Zr_{1-x}Al_xN$, and (f) $Hf_{1-x}Al_xN$. The B_k and B4-related minima correspond to $c/a \approx 1.2$ and ≈ 1.6, respectively. The black solid and dashed lines demonstrate how the energy profiles change under compressive ($p>0$) and tensile ($p<0$) pressures.

phase spontaneously relaxes to the B_k structure. This can be also seen in Fig. 5d where the difference between the absolute minimum energy (i.e. in this case the B_k structure) and a minimum energy for a given c/a ratio (i.e. minimum over a range of volumes), ΔE_{hex}, is plotted. There, one sees that a clear minimum is obtained around $c/a \approx 1.25$ while the energy curve only flattens around 1.6 (i.e. the supposed wurtzite structure). As the AlN mole fraction is increased in $Ti_{1-x}Al_xN$, the wurtzite-related minimum develops for $x=0.6875$ and finally for $x=0.75$ it is energetically preferable to the B_k structure. One should note, however, that for $x \leq 0.7$ where the B_k minimum dominates, the overall energy minimum is obtained for the cubic phase according to the energy of formation (Fig. 3).

The situation is quite different for $Zr_{1-x}Al_xN$ and $Hf_{1-x}Al_xN$ systems. There, for $x=0.625$ a broad minimum develops suggesting that a variety of structures (with different c/a ratios and volumes) can co-exist (see Fig. 5b and c). This, in turn, can rationalise the experimental observations of a broad dual-phase region by noticing that the hexagonal phase seems to be quite flexible (in terms of its structural parameters) and thus may adapt to the cubic phase. The hexagonal B_k minimum gets better defined for lower x. The black solid and dashed lines show how the energy profiles change with applied pressure. Clearly, the tensile pressure ($p<0$, solid line) makes the energy differences between the B_k and the wurtzite phases significantly smaller (see, e.g. $x=0.5625$ for $Zr_{1-x}Al_xN$ or $Hf_{1-x}Al_xN$). On the other hand, compressive

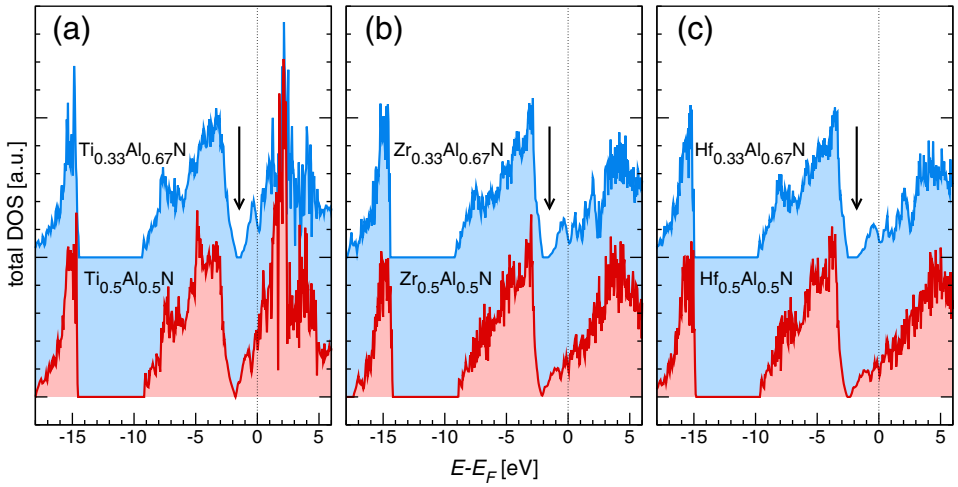

Fig. 6. Total density of states of cubic modifications of (a) $Ti_{1-x}Al_xN$, (b) $Zr_{1-x}Al_xN$, and (c) $Hf_{1-x}Al_xN$ for $x=0.5$ and $x=0.67$. The pseudo-gap at ≈−2 eV below the Fermi level opens at lower Al contents for the systems $Ti_{1-x}Al_xN$, $Zr_{1-x}Al_xN$, and HfAlN, respectively.

pressure ($p>0$, dashed line) promotes the similarity of these two phases at higher AlN content. Since stresses, although more complex than hydrostatic pressure used here for the demonstration purposes, are present in real materials (due to the deposition process, polycrystalline nature of the films, etc.) we expect that the hexagonal phase possesses similar flexibility also for AlN mole fractions of ≈0.5, where the cubic and hexagonal B_k energies of formation overlap (see Fig. 3). In general, the co-existence of the hexagonal phases, and the broad range of structures that can co-exist for some compositions, is a result of a competition between the four co-ordinated sp^3 bonding in AlN and the five co-ordinated sp^3d hybridisation that would take place in TMN hexagonal phases. The local compositional fluctuation cause one or other scheme to be locally preferred, similar to what has been discussed for the $Nb_{1-x}Al_xN$ system [7].

An additional observation from the energy profiles in Fig. 5d–f is that the onset of the wurtzite phase shifts to lower AlN mole fractions when changing from $Ti_{1-x}Al_xN$ to $Zr_{1-x}Al_xN$ to $Hf_{1-x}Al_xN$.

4.3. Density of states

In our previous study focusing on the NbN–AlN system [7] we pointed out, that the onset of the wurtzite phase is correlated with an opening of a pseudo-gap at ≈−2 eV below the Fermi level, E_F, in the total density of states (DOS). A similar conclusion can be drawn from the DOS of the $Ti_{1-x}Al_xN$, $Zr_{1-x}Al_xN$, and $Hf_{1-x}Al_xN$ systems plotted in Fig. 6. The pseudo-gap for $Ti_{1-x}Al_xN$ is closed for $x=0.5$ while it is slightly opened for $x=0.67$ (see Fig. 6a). A similar situation is also for the $Zr_{1-x}Al_xN$ where the pseudo-gap is, however, wider opened for $x=0.67$ as compared with $Ti_{0.33}Al_{0.67}N$ (Fig. 6b). In the case of $Hf_{1-x}Al_xN$, the opening of the pseudo-gap is signalled already at $x=0.5$; for $Hf_{0.33}Al_{0.67}N$, the pseudo-gap is opened to more than 1 eV (Fig. 6c).

A similar observation was made by Alling and co-workers [20, 21] for $Ti_{1-x}Al_xN$. The authors argued that the pseudo-gap opening is related to a localisation of the Ti-*d* orbitals, which are the states exclusively contributing to the DOS in the region ≈−2–0 eV below the Fermi level. This localisation causes a weakening of the overall bonding (by breaking the metallic anion–anion interactions), and a change of the hybridisation scheme from the octahedral six-coordinated sp^3d^2 and five-coordinated sp^3d to the tetrahedral four-coordinated sp^3 [36]. The changes in (projected) density of states as well as charge density maps are similar to those previously reported for the NbN–AlN system [7]. The same mechanism is responsible also for opening of the pseudo-gap also in $Zr_{1-x}Al_xN$ and $Hf_{1-x}Al_xN$

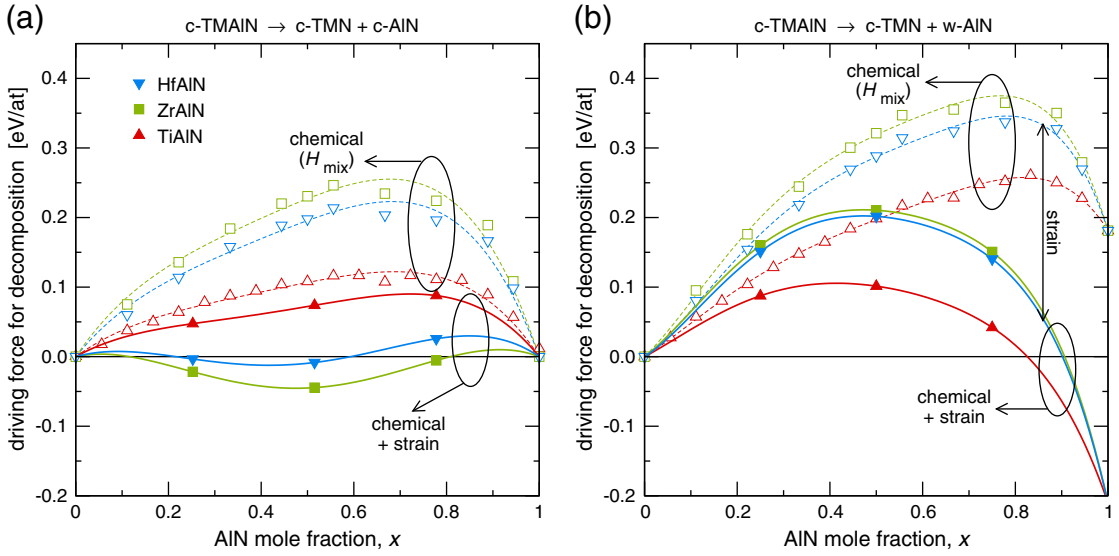

Fig. 7. Calculated chemical and total (chemical + strain components) driving force for decomposition of the c-TM–Al–N into (a) c-TMN and c-AlN, and (b) c-TMN and w-AlN compounds.

systems which explains why the pseudo-gap appearance is correlated with the onset of the four-coordinated wurtzite structure.

4.4. Driving force for the decomposition of the metastable phases

Since the energy of formation curves are bowed upwards in Fig. 3, the mixing enthalpy with respect to the binary boundary systems is positive, meaning all three systems ({Ti,Zr,Hf}–Al–N), and in particular the cubic alloys, are metastable. The dashed lines in Fig. 7a and b present the mixing enthalpies for the cubic ternaries calculated with respect to the cubic and stable binary compounds, i.e. w-AlN and c-AlN, respectively, and c-TiN, c-ZrN, or c-HfN. This part is regarded as the chemical driving force for decomposition of the metastable ternary alloys, and is the smallest for $Ti_{1-x}Al_xN$, followed by $Hf_{1-x}Al_xN$ and $Zr_{1-x}Al_xN$.

A model considering the kinetics of decomposition including the strain energy has been developed by Mayrhofer et al. [37]. Höglund et al. [38] introduced a simplified static approach, in which the strain-related part for the decomposition driving force can be estimated. If one assumes the starting state (ternary alloy) is unstrained, then due to a volume difference between the binary phases, and due to non-Vegard-like behaviour of the alloy volume, the binary compounds will be strained in the final state. Consequently, in such a model, the strain energy cost goes against the energy gain expressed as the chemical driving force.

The experimental evidence for spinodal decomposition in $Ti_{1-x}Al_xN$ [39, 40], $Zr_{1-x}Al_xN$ [32, 41] and most recently also for $Hf_{1-x}Al_xN$ [42] is well supported by theory [4, 20, 43]. The chemical driving force for decomposition into binary cubic nitrides is relevant in particular for the spinodal isostructural decomposition. The dashed lines in Fig. 7a show that H_{mix} is about twice as big in $Zr_{1-x}Al_xN$ and $Hf_{1-x}Al_xN$ than it is for $Ti_{1-x}Al_xN$, suggesting there will be higher driving force for the isostructural decomposition in $Zr_{1-x}Al_xN$ and $Hf_{1-x}Al_xN$ than in $Ti_{1-x}Al_xN$ around the c-AlN solubility limit. When an isostructural decomposition with coherent phases is taken into account [38], than the strain energy introduced in the binary phases decreases the driving force for decomposition. This is shown in Fig. 7a with solid lines. Interestingly, the assumption of coherent phases lower the driving force only slightly in $Ti_{1-x}Al_xN$, while it decreases it to essentially zero or less for $Zr_{1-x}Al_xN$ and $Hf_{1-x}Al_xN$. The reason for this behaviour is the much larger lattice mismatch between ZrN/AlN and HfN/AlN than between TiN/AlN. Consequently, the isostructural decomposition starts earlier in $Zr_{1-x}Al_xN$ and $Hf_{1-x}Al_xN$ than in $Ti_{1-x}Al_xN$ due to higher driving force for zero or small coherency stress, while when the concentration fluctuation increases, the spinodal isostructural decomposition in $Zr_{1-x}Al_xN$ and $Hf_{1-x}Al_xN$ is likely to slow down more than in $Ti_{1-x}Al_xN$ due to the coherency strains.

A similar situation is obtained also for evaluating the driving forces for decomposition into the stable binary constituents, c-TMN and w-AlN (Fig. 7b). Here, due to the huge volume mismatch between the c-AlN and w-AlN, a stabilisation of the cubic phase against the decomposition is obtained at the AlN-rich end.

5. Conclusions

The paper presents a comprehensive study of the structural properties and phase stability of cubic B1, hexagonal B_k, and wurtzite B4 allotropes in the ternary $Ti_{1-x}Al_xN$, $Zr_{1-x}Al_xN$, and $Hf_{1-x}Al_xN$ systems. For all systems, a deviation from the linear Vegard-like behaviour is predicted for the lattice constants. While the cubic and hexagonal B_k phases exhibit a positive bowing (i.e. the alloy has a bigger volume than the mixture of respective binary compounds), the wurtzite phase obeys a negative bowing.

The B1 cubic $Ti_{1-x}Al_xN$ alloy is predicted to be stable up to ≈ 0.7, for higher AlN mole fraction the wurtzite phase is energetically favourable. In the case of $Zr_{1-x}Al_xN$ and $Hf_{1-x}Al_xN$, the cubic phases are favourable up to ≈ 0.45, followed by a broad dual-phase cubic and hexagonal B_k mixture up to ≈ 0.68 and ≈ 0.62, respectively. It is also possible that due to the higher driving forces in $Zr_{1-x}Al_xN$ and $Hf_{1-x}Al_xN$ as compared to $Ti_{1-x}Al_xN$, the spinodal decomposition starts at lower temperatures in this transition region but also the formation of w-AlN is preferred. For higher AlN mole fractions, the wurtzite phase is predicted to be the most stable one. The predictions agree well with the experimental findings presented in the literature before as well as with the experimental results shown here.

The onset of the wurtzite phase is correlated with the opening of a pseudo-gap ≈ -2 eV below the Fermi level. This has been ascribed to the localisation of the TM *d*-states and a subsequent change in the hybridised bonding schemes.

Acknowledgements

Financial support by the START Program (Y371) of the Austrian Science Fund (FWF) is greatly acknowledged.

References

[1] S. PalDey, S.C. Deevi, Mater. Sci. Eng. A 342 (2003) 58.
[2] P.H. Mayrhofer, A. Hörling, L. Karlsson, J. Sjolen, T. Larsson, C. Mitterer, L. Hultman, Appl. Phys. Lett. 83 (2003) 2049.
[3] H. Holleck, Surf. Coat. Technol. 36 (1988) 151.
[4] S. Sheng, R. Zhang, S. Vepřek, Acta Mater. 56 (2008) 968.
[5] H.-S. Seo, T.-Y. Lee, I. Petrov, J.E. Greene, D. Gall, J. Appl. Phys. 97 (2005) 083521.
[6] B. Howe, J. Bareño, M. Sardela, J. Wen, J. Greene, L. Hultman, A. Voevodin, I. Petrov, Surf. Coat. Technol. 202 (2007) 809.
[7] D. Holec, R. Franz, P.H. Mayrhofer, C. Mitterer, J. Phys. D: Appl. Phys. 43 (2010) 145403.
[8] C. Höglund, J. Birch, B. Alling, J. Bareno, Z. Czigany, P.O.A. Persson, G. Wingqvist, A. Zukauskaite, L. Hultman, J. Appl. Phys. 107 (2010) 123515.
[9] S.-H. Wei, L.G. Ferreira, J.E. Bernard, A. Zunger, Phys. Rev. B 42 (1990) 9622.
[10] L. Chen, D. Holec, Y. Du, P.H. Mayrhofer, Thin Solid Films 519 (2011) 5503.
[11] D. Holec, Multi-scale Modelling of III-Nitrides: Selected Topics from Dislocations to the Electronic Structure, VDM Verlag, 2010.
[12] G. Kresse, J. Hafner, Phys. Rev. B 47 (1993) 558.
[13] G. Kresse, J. Furthmüller, Phys. Rev. B 54 (1996) 11169.
[14] G. Kresse, D. Joubert, Phys. Rev. B 59 (1999) 1758.
[15] Y. Wang, J.P. Perdew, Phys. Rev. B 44 (1991) 13298.
[16] P.H. Mayrhofer, M. Geier, C. Locker, L. Chen, Int. J. Mater. Res. 100 (2009) 1052.
[17] P.H. Mayrhofer, F. Kunc, J. Musil, C. Mitterer, Thin Solid Films 415 (2002) 151.
[18] F. Birch, Phys. Rev. 71 (1947) 809.
[19] A. Flink, J. Andersson, B. Alling, R. Daniel, J. Sjolen, L. Karlsson, L. Hultman, Thin Solid Films 517 (2008) 714.
[20] B. Alling, A.V. Ruban, A. Karimi, O.E. Peil, S.I. Simak, L. Hultman, I.A. Abrikosov, Phys. Rev. B 75 (2007) 045123.
[21] B. Alling, A. Karimi, I.A. Abrikosov, Surf. Coat. Technol. 203 (2008) 883.
[22] P.H. Mayrhofer, D. Music, J.M. Schneider, J. Appl. Phys. 100 (2006) 094906.
[23] U. Wahlström, L. Hultman, J.E. Sundgren, F. Adibi, I. Petrov, J.E. Greene, Thin Solid Films 235 (1993) 62.
[24] R.F. Zhang, S. Vepřek, Mater. Sci. Eng. A 448 (2007) 111.
[25] D. Holec, F. Rovere, P.H. Mayrhofer, P. Barna, Scr. Mater. 62 (2010) 349.
[26] Y. Makino, Surf. Coat. Technol. 193 (2005) 185.
[27] R. Prange, R. Cremer, D. Neuschütz, Surf. Coat. Technol. 133–134 (2000) 208.
[28] S.-H. Lee, B.-J. Kim, H.-H. Kim, J.-J. Lee, J. Appl. Phys. 80 (1996) 1469.
[29] K. Kutschej, P. Mayrhofer, M. Kathrein, P. Polcik, R. Tessadri, C. Mitterer, Surf. Coat. Technol. 200 (2005) 2358.
[30] R. Lamni, R. Sanjines, M. Parlinska-Wojtan, A. Karimi, F. Levy, J. Vac. Sci. Technol. A 23 (2005) 593.
[31] H. Hasegawa, M. Kawate, T. Suzuki, Surf. Coat. Technol. 200 (2005) 2409.
[32] L. Rogström, L. Johnson, M. Johansson, M. Ahlgren, L. Hultman, M. Odén, Thin Solid Films 519 (2010) 694.
[33] R. Franz, C. Mitterer, M. Lechthaler, C. Polzer, J. Vac. Sci. Technol. A 28 (2010) 528.
[34] B. Howe, E. Sammann, J. Wen, T. Spila, J. Greene, L. Hultman, I. Petrov, Acta Mater. 59 (2011) 421.
[35] F. Tasnádi, B. Alling, C. Häglund, G. Wingqvist, J. Birch, L. Hultman, I. Abrikosov, Phys. Rev. Lett. 104 (2010) 137601.
[36] P. Atkins, Physical Chemistry, Oxford University Press, 1998.
[37] P. Mayrhofer, F. Fischer, H. Böhm, C. Mitterer, J. Schneider, Acta Mater. 55 (2007) 1441.
[38] C. Höglund, B. Alling, J. Birch, M. Beckers, P.O.A. Persson, C. Baehtz, Z. Czigány, J. Jensen, L. Hultman, Phys. Rev. B 81 (2010) 224101.
[39] R. Rachbauer, E. Stergar, S. Massl, M. Moser, P. Mayrhofer, Scr. Mater. 61 (2009) 725.
[40] R. Rachbauer, S. Massl, E. Stergar, D. Holec, D. Kiener, J. Keckes, J. Patscheider, M. Stiefel, H. Leitner, P.H. Mayrhofer, J. Appl. Phys. 110 (2011) 023515.
[41] R. Sanjinés, C. Sandu, R. Lamni, F. Lévy, Surf. Coat. Technol. 200 (2006) 6308.
[42] B. Howe, T. Oates, S. Puttnam, M. Sardela, A. Voevodin, H. Arwin, J. Greene, L. Hultman, I. Petrov, International Conference of Metallurgical Coatings and Thin Films (ICMCTF), 2-5 April 2011, San Diego, USA.
[43] P.H. Mayrhofer, D. Music, J.M. Schneider, Appl. Phys. Lett. 88 (2006) 071922.